

PAPER

## 2D laser-collision induced fluorescence in low-pressure argon discharges

To cite this article: E V Barnat and B R Weatherford 2015 *Plasma Sources Sci. Technol.* **24** 055024

### Manuscript version: Accepted Manuscript

Accepted Manuscript is "the version of the article accepted for publication including all changes made as a result of the peer review process, and which may also include the addition to the article by IOP Publishing of a header, an article ID, a cover sheet and/or an 'Accepted Manuscript' watermark, but excluding any other editing, typesetting or other changes made by IOP Publishing and/or its licensors"

This Accepted Manuscript is© .

During the embargo period (the 12 month period from the publication of the Version of Record of this article), the Accepted Manuscript is fully protected by copyright and cannot be reused or reposted elsewhere.

As the Version of Record of this article is going to be / has been published on a subscription basis, this Accepted Manuscript will be available for reuse under a CC BY-NC-ND 3.0 licence after the 12 month embargo period.

After the embargo period, everyone is permitted to use copy and redistribute this article for non-commercial purposes only, provided that they adhere to all the terms of the licence <https://creativecommons.org/licenses/by-nc-nd/3.0>

Although reasonable endeavours have been taken to obtain all necessary permissions from third parties to include their copyrighted content within this article, their full citation and copyright line may not be present in this Accepted Manuscript version. Before using any content from this article, please refer to the Version of Record on IOPscience once published for full citation and copyright details, as permissions may be required. All third party content is fully copyright protected, unless specifically stated otherwise in the figure caption in the Version of Record.

View the [article online](#) for updates and enhancements.

**Manuscript version: Accepted Manuscript**

The “**Accepted Manuscript**” is the author’s original version of an article including any changes made following the peer review process but excluding any editing, typesetting or other changes made by IOP Publishing and/or its licensors.

During the embargo period (the 12 month period from publication of the Version of Record of this article), the Accepted Manuscript:

- is fully protected by copyright and can only be accessed by subscribers to the journal;
- cannot be reused or reposted elsewhere by anyone unless an exception to this policy has been agreed in writing with IOP Publishing



As the Version of Record of this article is going to be/has been published on a subscription basis, this Accepted Manuscript will be available for reuse under a [CC BY-NC-ND 3.0](#) licence after a 12 month embargo period.

After the embargo period, everyone is permitted to copy and redistribute this article for Non-Commercial purposes only, provided they\*:

- give appropriate credit and provide the appropriate copyright notice;
- show that this article is published under a CC BY-NC-ND 3.0 licence;
- provide a link to the CC BY-NC-ND 3.0 licence;
- provide a link to the Version of Record;
- do not use this article for commercial advantage or monetary compensation; and
- only use this article in its entirety and do not make derivatives from it.

\*Please see CC BY-NC-ND 3.0 licence for full terms.

View the Version of Record for this article online at [iopscience.org](http://iopscience.org)

1  
2  
3  
4  
5  
6  
7  
8  
9  
10  
11  
12  
13  
14  
15  
16  
17  
18  
19  
20  
21  
22  
23  
24  
25  
26  
27  
28  
29  
30  
31  
32  
33  
34  
35  
36  
37  
38  
39  
40  
41  
42  
43  
44  
45  
46  
47  
48  
49  
50  
51  
52  
53  
54  
55  
56  
57  
58  
59  
60

# Two dimensional laser-collision induced fluorescence in low-pressure argon discharges

E. V. Barnat<sup>1</sup> and B. R. Weatherford<sup>2</sup>

- <sup>1)</sup> Sandia National Laboratories, Albuquerque, NM 87185-1423, USA
- <sup>2)</sup> L-3 Communications, Electron Devices Division, 960 Industrial Road, San Carlos, CA 94070.

## Abstract

Development and application of laser-collision induced fluorescence (LCIF) diagnostic technique is presented for the use of interrogating argon plasma discharges. Key atomic states of argon utilized for the LCIF method are identified. A simplified two-state collisional radiative model is then used to establish scaling relations between the LCIF, electron density, and reduced electric fields (E/N). The procedure used to generate, detect and calibrate the LCIF in controlled plasma environments is discussed in detail. LCIF emanating from an argon discharge is then presented for electron densities spanning  $10^9$  e/cm<sup>3</sup> to  $10^{12}$  e/cm<sup>3</sup> and reduced electric fields spanning 0.1 Td to 40 Td. Finally, application of the LCIF technique for measuring the spatial distribution of both electron densities and reduced electric field is demonstrated.

## I. Introduction

*[Overview of challenging plasma systems]*

Low-temperature (< 10 eV), low pressure (< 10 Torr) plasma discharges can exhibit complex structure that varies over spatial scales comparable to the Debye length (< 10  $\mu$ m) but may be utilized to fill large volumes (> 1 m). Likewise, these plasma discharges are governed by dynamic behavior that span timescales associated with plasma generation (< 10 ns) and thermal transport (> 10 s). This range of scales persistently challenges the capabilities of any one diagnostic. Therefore, there is a continual need to develop more flexible diagnostic methods that can respond to these spans of spatial and temporal timescales.

Many plasma applications benefit from the development of improved diagnostics which address these spans of time and spatial scales. One such example is the formation and fabrication of micro-electronic devices using large area (meter-scaled systems), capacitively coupled, radio frequency driven plasmas. In these well studied systems, oscillating sheaths (~ 1 mm thick) can drive currents and induce

electromagnetic effects that significantly impact where energy is deposited in the discharge<sup>1 2</sup>. Such effects can lead to non-uniform plasma profiles that extend across the processing area (100s of mm) and result in non-uniform processing of the targeted devices<sup>3 4 5 6</sup>. Furthermore, yields may also be affected by discontinuities present at the edge of the processed material or diffusional transport to the walls<sup>7</sup>. While considerable effort has been spent on mitigating these effects, the large aspect-ratio of the chamber (large diameter, small electrode spacing) and radio-frequency environment makes the interrogation of such plasma systems a significant challenge. Many of the diagnostics used to better understand these discharges are based on line-of-sight methods including variations of optical emission spectroscopy<sup>8 9</sup>, (laser diode) absorption spectroscopy<sup>10 11</sup> or microwave interferometry<sup>12 4</sup>. While these powerful methods provide important insight into the physics governing these discharges, they often require assumptions about the processes which generate the observed quantities of interest (light emitted from the plasma) or the symmetry or structure of the discharge.

Diagnostic methods such as planar laser induced fluorescence<sup>13 14 15 16</sup>(PLIF), planar laser-collision induced fluorescence<sup>17 18 19</sup> (PLCIF) and planar laser induced fluorescence-dip<sup>20 21 22 23 24</sup>(PLIF-dip) spectroscopy constitute a category of optically active diagnostic techniques<sup>25</sup> that provide high spatial (10s  $\mu\text{m}$ ) and high temporal (10s ns) resolution images of plasma species, electron densities, and electric fields and are less constrained by such assumptions. For example, PLIF utilizes a planar sheet of laser tuned to a specific atomic or molecular transition that illuminates the interrogated region. Fluorescence is generated by the relaxation of the targeted species and is then measured by a photodetector or imaged by a camera. PLCIF is a variation of the PLIF technique which measures fluorescence from near-by states (populated through collisions) and PLIF-dip utilizes a second laser to displace some of the excited target species to Stark-shifted Rydberg states. While LIF and LIF-dip based techniques have been developed and demonstrated for a broad array of discharge gases, LCIF based techniques have received considerably less development. As argon is utilized across a broad range of plasma based applications, it is desirable to develop extend the LCIF method so that it can be utilized for these applications. With a few notable exceptions<sup>26 27 28 29</sup>, most of the development and application of the LCIF technique as a method to assess electron density has been performed in helium discharges<sup>30 31</sup>.

In this paper, the development and application of the planar LCIF technique as a diagnostic of electron density and “electron temperature” is described for low temperature, low pressure plasmas generated with argon. While various forms of the LCIF technique have been demonstrated in the argon environment<sup>29 37 38 39 40</sup>, the bulk of these studies focused on quantifying either the relaxation rate of the laser excited state or the repopulation rate of the laser-depleted state due to collisions with the plasma species (neutrals and electrons). The study performed by Stewart and Smith<sup>29</sup> utilized a continuous-wave (cw) variation of the LCIF method as a means of assessing electron temperatures. Therefore, emphasis in this work is placed on fast (< 10 nanoseconds) laser excitation of higher  $3p_2$  states which more readily couple into ( $3s$ ,  $4s$  and  $4d$ ) states which radiate in the visible spectrum. As a result of employing the proposed excitation and monitoring scheme, the LCIF technique is readily applicable to the spatial and temporal characterization of an argon-containing plasma discharge.

The paper is outlined as follows. In Section II, an overview of the LCIF technique is presented and a simplified two-state model is utilized to predict key scaling trends of the LCIF signal emanating from various argon states as functions of electron density and electron temperature. As electron temperature is usually difficult to properly define or ascertain, scaling trends are also presented as a function of the electric field present in the plasma column that energize or heat the electrons. More specifically, trends in the reduced electric field ( $E/N$  – electric field divided by neutral gas density) are constructed as the parameter  $E/N$  is often used to describe electron properties. Furthermore, kinetic simulations can use  $E/N$  as an input to compute anticipated electron energy distributions as well as effective electron temperatures. In Section III, a discussion of the setup and calibration procedure is provided. This discussion includes a description of the hardware utilized for plasma generation and manipulation, methodology utilized to characterize both the electron density and the reduced electric field ( $E/N$ ) in the plasmas, the optical system utilized to produce and monitor both the LIF and LCIF emanating from the plasma after laser excitation and finally, the procedure to control both the density and  $E/N$  to properly calibrate the LCIF diagnostic. In Section IV, key LCIF scaling trends are presented as functions of both electron density and  $E/N$  while in Section V, application of the LCIF technique to measure plasma formation above a magnetized electrode immediately after the electrode is biased. Finally, in Section VI, a summary of the paper and paths forward to extend the LCIF diagnostic are offered.

**II. Proposed LCIF scheme in argon and two-state model**

Laser-collision induced fluorescence (LCIF) is an extension of the more conventional laser induced fluorescence (LIF) technique. Both techniques employ a laser to excite an atom in a plasma discharge from a lower-lying targeted state to an intermediate state. In conventional LIF, the radiation emitted from the atom as it transitions from the intermediate state to a lower state (typically different than the original target state) can be detected to qualitatively indicate the presence of this target state. In some instances the magnitude of LIF signal can be utilized as a measure of absolute densities of the target state. In addition to monitoring the LIF from the intermediate excited species, LCIF also involves monitoring the emissions emanating from energetically close, but “uphill” states. These uphill states are populated through collisions between the laser excited species and energetic plasma species. The magnitude of the emissions from these collision-populated states, or collision induced fluorescence (LCIF), serves as a measure of the interaction between the laser-excited species and energetic plasma species capable of driving the transition.

***IIa Proposed LCIF scheme in argon***

A simplified energy level diagram indicating the key target transitions utilized in this study is presented in Figure 1 while a list of their key properties (wavelength, radiation rate ( $A$ ) and energy above laser excited state ( $\Delta E$ )) are presented in Table 1. A laser is used to excite argon atoms out of the lowest lying  $1s_5$  metastable state and into a higher lying  $3p_2$  state. While stronger transitions between

the 1s and 3p manifold exists, the 3p<sub>2</sub> state is a convenient state to excite as it is near the top of the 3p manifold and therefore in close proximity (energetically) but still lays below the 3s and 4d states that source the 590 nm to 690 nm LCIF signals. Furthermore, there is good spectral separation between the 394.9 nm light used for excitation and the 433.5 nm LIF emitted from the laser-excited state. Target transitions of interest that generate LCIF include 4d<sub>5</sub> → 2p<sub>10</sub> at 687.13 nm ( $\Delta E = 0.024$  eV), 4d<sub>3</sub> → 2p<sub>10</sub> at 675.28 nm ( $\Delta E = 0.055$  eV), 3s<sub>5</sub> → 2p<sub>10</sub> at 641.63 nm ( $\Delta E = 0.152$  eV) and 4s'<sub>1</sub> → 2p<sub>10</sub> at 591.21 nm ( $\Delta E = 0.316$  eV) and are listed in Table 1 along with additional lines that are in close spectral proximity. Some of these additional lines are observed and will be discussed in Section IV. While not an exhaustive list, the targeted transitions have different energy separation above the laser excited state, and therefore serve as potential candidates to test for electron-temperature sensitive transitions.

### ***IIb Two state model to simulate LCIF***

A collisional radiative model can be used to predict the temporal evolution of a laser-excited species and one of the states targeted for LCIF. The model can be expressed as a system of coupled equations that take the form of

$$\frac{dN_j}{dt} = \left[ \sum_{i>j} A_{ij} N_i - \sum_{i<j} A_{ji}^j N_j \right] + \left[ \sum_{i \neq j} K_{ij}^e N_i - \sum_{i \neq j} K_{ji}^e N_j \right] n_e + \sum_k \left[ \sum_{i \neq j} K_{ikj}^a N_i - \sum_{i \neq j} K_{jki}^a N_j \right] N_k, \quad (1)$$

where  $N_j$  is the population of a given state,  $A_{ij}$  is the radiative rate between two states,  $K_{ij}^e$  represents the electron-driven collision rate coefficient between two states, and  $K_{ijk}^a$  represents the atomic or neutral-driven collision rate coefficient between two states. Collision rate coefficients  $K_{ij}^x$  are computed using

$$K_{ij}^x = \langle \sigma_{ij}(E) v_x(E) f(E) \rangle, \quad (2)$$

which represents a weighted average of the energy dependent cross-section,  $\sigma_{ij}(E)$  that serves to describe the strength or probability of the interaction, and the velocity of the particle,  $v_x$ , interacting with the given state. Weighting of the average is provided through the function  $f(E)$  which is a normalized probability distribution describing the likelihood that a particle has an energy  $E$ . The right-hand side of Eq. 1 is arranged into three terms consisting of photon-driven interactions (the first term), electron driven interactions (second term) and atomic or neutral driven interactions (third term). Each term consists of a populating (positive) term that is proportional to another state,  $i$ , and a loss (negative) term that is proportional to the given state,  $j$ . The evolution of the system in response to laser excitation is therefore dependent on the competition between these various interactions.

As has been discussed in other treatments that utilize collisional radiative models, considerable complication can arise in assessing the strength of the various interactions due to uncertainties in factors such as the explicit functional forms of either the distribution of electron energies or the energy dependence of the cross-sections which connect various excited states in argon. For example, in the work of Bogaerts et al<sup>41</sup>, 65 states are generated to form a “condensed” set out of many more levels

that exists in the argon manifold and functional forms of the cross-sections that connect the various upper states (such as the  $3p_2$  to  $3d$  and  $5s$  states) are utilized due to lack of availability of more accurate cross-sections. Therefore, in this study a two state model is utilized to compute interactions between the laser-excited state and the state emanating the LCIF. Because of this simplification, results generated from this model are not intended to be predictive, but indicative. That is, the trends derived from these simulations will be used to discuss the observed LCIF trends that will be presented in Section IV but a direct comparison between predicted results and measured results will not be offered.

A central piece of physics to be captured by this two-state model is the role the electron temperature plays in the population kinetics as the energy spacing between the excited state and target LCIF-generating state increases. To capture this element, energy-dependent cross-sections recommended by Bogaerts<sup>41</sup> are used. These cross-sections take the functional form of

$$\sigma(E) = 4\pi a_0^2 \alpha \left(\frac{E}{\Delta E}\right)^n \left(\frac{E}{\Delta E} - 1\right) \ln\left(1.25\beta \frac{E}{\Delta E}\right), \quad (3)$$

where  $a_0$  is the Bohr radius,  $E$  is the energy of the electron,  $\Delta E$  is the energy between the laser excited state and the higher energy level excited by the electron impact event. A fitting parameter,  $\alpha$ , dictates the magnitude of the cross-section. The parameters  $n$  and  $\beta$  dictate the decay of the cross-section as the electron energy exceeds the threshold energy of the interaction. Electron temperature dependent collisional rates are constructed using Eq. 2, the functional form of the cross-section as outlined in Eq. 3, and a Maxwellian distribution for the electrons. Energy dependent cross-sections evaluated for two of the transitions of interest ( $\Delta E = 0.02$  eV, black curves, and  $\Delta E = 0.15$  eV, red curves) are presented in Figure 2a while evaluated temperature dependent rate coefficients are presented in Figure 2b. For both transitions values of  $\alpha = 2000$  and  $\beta = 0.8$  were used as they yielded peak values of the cross-sections that are comparable to values suggested by Yanguas-Gil *et al*<sup>42</sup>. The solid curves correspond to  $n = 2$  as was initially proposed in Bogaerts<sup>41</sup>, and the dashed curves utilize a slightly reduced value of 1.75. Using  $n = 2$ , the predicted rates for the  $4d_5$  transition ( $\Delta E = 0.02$  eV) decrease for electron temperatures over  $\sim 0.3$  eV. Comparatively, the predicted rates for the same transition using  $n = 1.75$  vary little with electron temperatures above 0.3 eV. Similar temperature dependent trends are also observed for the  $3s_5$  transition ( $\Delta E = 0.15$  eV). As will be apparent in the discussion of the observed LCIF trends in Section IV, the latter functional form ( $n = 1.75$ ) produces rates that are more consistent with the observed trends. Estimates of  $\alpha$  are best assessed by comparing the predicted intensities of the LCIF signal (typically normalized to the LIF from the laser excited state) to measured LCIF signals (likewise normalized to the LIF from the laser excited state) and will be further discussed in Section IV.

In addition to electrons, collisions with energetic neutrals can populate the LCIF emitting state. The contribution of this interaction depends on the effective cross-section of the colliding partners (which are typically treated as hard spheres) and the number of the particles capable of driving such a transition. For example, gas particles near room temperature ( $T_g = 300$  K) have an average energy of 0.04 eV, greater than energy spacing between the  $3p_2$  state and the  $4d_5$  state ( $\Delta E = 0.024$  eV), but less than the energy spacing between the  $3p_2$  state and the  $4d_3$  state ( $\Delta E = 0.053$  eV). Therefore it is anticipated that the  $4d_5$  state will be populated at a higher rate by neutral collisions from the  $3p_2$  state

than the more isolated  $4d_3$  state. As the energy spacing between the  $3p_2$  state and the targeted LCIF state increase, it is expected that the contribution of population transfer by energetic neutrals should decrease and the functional form of the atomic induced collisional rate will scale as

$$K_{ij}^a = 4\gamma\pi a_0^2 \sqrt{\frac{8kT_g}{\pi M_g}} e^{-\Delta E/kT_g}, \quad (4)$$

where  $\gamma$  is a factor that scales the magnitude of the cross-section and  $M_g$  is the mass of the argon atoms. Values of  $K_{ij}^a$  are anticipated to be on the order of  $10^{-10} \text{ cm}^3/\text{s}$ <sup>38 39</sup>.

Using these rates, along with the known radiation coefficients<sup>43</sup>, the two-state collisional radiative model is solved after an emulated laser excitation from the  $1s_5$  to  $3p_2$  state. Representative solutions of the time evolution of the LIF emanating from the  $3p_2$  state at 433 nm and the LCIF emanating from the collision-populated  $4d_3$  state at 675 nm are presented for three different electron densities in Figure 3. For these calculations, the neutral collisions are ignored and an electron temperature of  $\sim 1 \text{ eV}$  is assumed. The (normalized) scaling trends with the electron density, electron temperature, and reduced electric field are presented in Figure 4. The time resolved trends plotted in Figure 3 and the electron density dependent scaling trends in Figure 4a convey a key feature of the LCIF diagnostic. Under ideal circumstances, as the electron density increases, the magnitude of the LCIF increases at a nearly linear rate (solid black line, Figure 4a). Deviations from this linearity manifest in two ways.

First, at lower densities, collisions with neutrals can contribute to the population of the LCIF-emitting state particularly at higher neutral temperatures (Eq. 4). The broken blue lines in Figure 4a show the effect of these collisions. With sufficient neutral collisions the LCIF signal becomes independent of the electron density. At a pressure of 10 mTorr, neutral induced collisions are comparable to electron induced collisions when the electron density is  $2 \times 10^9 \text{ e/cm}^3$ . At a pressure of 100 mTorr, neutral induced collisions are comparable to electron induced collisions when the electron density is  $2 \times 10^{10} \text{ e/cm}^3$ . For both cases, the gas temperature is set to 300 K. Neutral induced collisions will be more prominent for smaller gap transitions, higher gas pressures, and higher gas temperatures.

The second process which limits the linearity of LCIF scaling with electron density is the depopulation of atoms in the LCIF-emitting state by processes other than radiative decay. If the loss rate from this state increases with no corresponding change in the loss rate of the LIF-emitting state, the LCIF trends again become independent of electron density at higher electron densities (broken red curves, Figure 4a). The magnitude of this effect scales with discrepancy in depopulation rates of the LIF and LCIF emitting states.

Electron temperature and reduced electric field ( $E/N$ ) scaling trends are presented in Figure 4b. The reduced electric field is correlated to the average electron energy ( $3/2kT_e$ ) through calculations performed with BOLSIG+<sup>44,45</sup> using the IST-Lisbon database for argon-electron cross-sections<sup>46</sup>. These trends illustrate a second key feature of the LCIF diagnostic. The temperature dependence of the collisional coupling has a strong dependence on the energy spacing between the two states (along with the the cross-section and the energy distribution of the electrons). In general, the LCIF signal, relative to



the LIF signal, is a strong function of electron temperature for temperatures around the threshold of the transition. At higher electron temperatures, the temperature dependence of the LCIF signal is not as strong. This behavior underlies the use of the LCIF diagnostic in measuring electron density and electron temperature.

For states energetically near the laser excited state such as the  $4d_5$  state, located 0.024 eV above the  $3p_2$  state, the temperature dependence of the LCIF signal is virtually flat over electron temperatures spanning 0.3-5 eV. Provided sufficiently low neutral collisions and depopulation of the LCIF-emitting states, these lower energy states provide a good measure of the electron density as they exhibit little to no dependence on the electron temperature. In contrast, the LCIF emanating from the higher lying 3s, 4s and 5s states around 591 nm is expected to show strong electron temperature dependence over the same 0.3 eV to 5 eV range and therefore serve as good transitions to assess the electron temperature. The specifics of the actual cross-sections will likely cause some deviation from the idealized trends illustrated here, therefore calibration of the LCIF technique is performed as will be described in the following sections.

### III. Setup and procedure utilized for calibrating LCIF scheme

The LCIF technique is calibrated in an argon discharge by the setup and procedure described in this section. The calibration cell, along with the means of characterizing the plasma generated in the cell is described in Section IIIa. Central to the calibration process is a double-pulse technique described in Section IIIb. As will be described in detail, this technique enables the ability to “tune” the plasma state for a desired density and a known drift velocity. The excitation and detection of target transitions outlined in the previous section are described in Section IIIc, and the procedure utilized to perform the LCIF calibration is described in Section IIId.

#### *IIIa Plasma chamber utilized for LCIF calibration*

Calibration of the proposed LCIF scheme is carried out using the setup illustrated in Figure 5. The plasma is contained within a 25.5 mm outer diameter, 20 mm inner diameter borosilicate glass tube which connects to an anode and to the host vacuum chamber. The chamber is pumped to pressures below 1 mTorr with a turbomolecular pump. While the ultimate pressure is not assessed, the residual rate of rise was less than 0.01 mTorr/minute. Argon gas is introduced into the chamber with a flow rate of 2 sccm and the pressure is controlled by a throttle valve in line between the turbomolecular pump and plasma chamber. LCIF calibration measurements presented in this study are performed at an argon pressure of 100 mTorr.

The plasma is characterized with the use of a cylindrical microwave resonant cavity that contains the 25 mm glass tube cavity, as illustrated in Figure 5. The resonant cavity is excited near the resonance of the  $TM_{010}$  mode ( $\nu_{\text{Resonance}} \sim 2.2$  GHz) by a small antenna located at the outer radius of the cavity. Electron densities ( $n_e$ ) and collision frequencies ( $\nu_c$ ) are determined by locating the shift and the

broadening of the resonance absorption due to the dielectric properties of the plasma<sup>47</sup>. To capture the shift and broadening of the resonant absorption, the microwave frequency is swept around the resonant frequency and the change in microwave energy coupled into the cavity is measured. The microwave absorption spectra allow the evaluation of the electron density evolution in response to induced changes in the plasma. In order to capture the fast variation of the plasma properties, a 1 GHz digitizing oscilloscope (WaveRunner 6100, Lecroy) is used to measure the change in absorption with respect to time for a single microwave frequency. The microwave frequency is then incremented and the process is repeated with the next voltage pulse. After a sufficient number of frequency steps, the microwave absorption spectra is reconstructed and the electron densities can be determined with the use of Eq. 5. The cavity is driven at  $\sim 1$  mW to avoid heating of the plasma by the microwaves. Error in measured electron density stems from assumptions on the distribution in the column. As this is not directly assessed, it is assumed that the electrons have a Bessel's like distribution that is peaked on axis and drops to zero at the walls. Deviations in this profile will modify peak electron densities, but not total electrons present in the interrogation volume.

In addition to assessing the density of the electrons with the resonant cavity, the density of argon atoms in the  $1s_5$  metastable state is monitored with laser diode absorption. For these measurements, a cw diode laser tuned to the  $1s_5 \rightarrow 2p_8$  transition (801.5 nm) passes through the resonant cavity, perpendicular to the axis of the tube (not shown). Absorption of the 801.5 nm light is detected with a fast photodiode and is recorded by the same digitizing oscilloscope used to monitor the microwaves coupled into the cavity. While not explicitly utilized in characterizing the plasma, the behavior of the metastable species (growth or accelerated decay) in response to the application of the second voltage pulse in the double-pulse technique is useful for benchmarking the assessment of electron heating.

### ***IIIb Plasma generation and manipulation using double-pulse technique***

Plasma is generated and then heated by using a double-pulse technique briefly described here. The initial high-voltage pulse (1000 to 3500 V, 5 to 20  $\mu$ s) applied to the isolated anode electrode via a current limiting resistor  $R_1$  (500 to 50 k $\Omega$ ) generates a plasma discharge. This first voltage pulse is referred to as the generating pulse. The electron density of the plasma discharge has a roughly linear correlation with the magnitude of the anode current (governed by the applied voltage and current limiting resistor). After the termination of the generating pulse (first pulse), a second voltage pulse (100 to 1000 V, 5  $\mu$ s long) is then applied to the anode via a second current limiting resistor  $R_2$  with values  $\sim \frac{1}{2}$  of the value of  $R_1$ . The second voltage pulse is referred to as the heating pulse. The delay time between the two pulses is  $\sim 80$   $\mu$ s while the repetition rate of plasma generation is 1 kHz. Two high-voltage generators (PVX-4140, IXYS) with  $< 25$  ns rise times are used to supply the two voltage pulses. A wide band current transducer (2100, Pearson Electronics) measures the current that flows through the plasma as a result of the applied voltage pulses

As the density of the plasma is governed by the first pulse (and hence “known”) the current drawn by the second pulse is used to heat the electron population. To assess the heating, the drift velocity ( $v_{Drift}$ ) is first determined by

$$v_{Drift} = \frac{I_2(t_0)}{en_e A_{Effective}}, \quad (5)$$

where  $I_2(t_0)$  is the current driven through the discharge by the application of the second pulse voltage as measured at the time of LCIF acquisition ( $t_0$ ) and  $A_{Effective}$  is the effective area over which the plasma is distributed in the glass tube. After determining the drift velocity, values of the reduced electric field (E/N) necessary to maintain the current flow through the discharge are extracted from published relations<sup>48 49 50 51</sup>. Average or characteristic electron energies are not explicitly obtained for this study.

To illustrate the manipulation and control of the plasma discharge through the application of the second pulse, characteristic scaling trends are plotted in Figure 6 as a function of applied voltage of the heating pulse. The current driven through the plasma scales with the applied amplitude of the heating pulse (Figure 6a). A transition in the rate of increase is observed to occur around 620 V. The change in the density of the  $1s_5$  species and electron densities between the beginning and end of the applied heating pulse are presented in Figure 6b. The change in the  $1s_5$  metastable species remains nearly constant for voltages below 600 V. Above 600 V, there is a sharp increase in metastable species that levels off at voltages exceeding 700 V. On the other hand, the electron densities exhibit increased loss with heating voltages below 720 V. With voltages above 720 V, the trend is reversed and the loss in electron density is reduced. Both the measured collision frequencies ( $\nu_c$ ) and calculated drift velocities ( $v_D$ ) are plotted in Figure 6c. The collision frequency remains constant for heating voltages less than 480 V and increase for heating voltages above 480 V whereas the drift velocity exhibits behavior similar to the current driven through the column by the heating voltage (Figure 6a). Finally, E/N values (extrapolated from  $v_D$ ) are plotted as function of heating voltage in Figure 6d. As was the case for both the current and the drift velocity, E/N exhibits monotonic increase with voltage and a transition in the rate of increase at approximately 700 volts.

To benchmark this procedure and to provide context to the trends presented in Figure 6, it is noted that the electron density reaches a balance between diffusional losses and ionization at 720 V. Equating the gain created by ionization to the losses through diffusion yields

$$v_{Ionization} = D_a \left( \frac{2.405}{R} \right)^2 = kT_i \mu_i \left( 1 + \frac{kT_e}{kT_i} \right) \left( \frac{2.405}{R} \right)^2, \quad (6)$$

where  $D_a$  is the ambipolar diffusion coefficient,  $R$  is the radius of the plasma containing glass tube,  $\mu_i$  is the ion mobility, and  $kT_i$  and  $kT_e$  are the ion and electron temperatures<sup>52</sup>. The behavior of the production and loss rates are plotted as functions of E/N and electron temperature in Figure 7a using available ionization rates and assuming an E/N independent  $\mu_i$  of  $2 \times 10^{-4} \text{ m}^2/\text{Vs}$ <sup>44 45 46</sup>. As indicated by the figure, diffusional loss dominates charge balance for lower values of E/N whereas ionization gain dominates charge balance for higher values of E/N. Equilibrium between production and loss is predicted to occur at an E/N value of  $\sim 14 \text{ Td}$ , comparable to the measured E/N value of  $19 \text{ Td}$ . As the

energy threshold for metastable species generation is lower than ionization, net production of metastables occurs at a lower (measured) E/N value of 12 Td. Transitions in the voltage dependent slope of current (Figure 6a), drift velocity (Figure 6c) and E/N (Figure 6d) occurs when electron generation equals and exceeds electron loss. While it is expected that the collision frequency (Figure 6c) likewise increase with applied voltage (Figure 7b), this is not observed for applied voltages below 470 V ( $\sim 9$  Td). Instead, the collision frequency remains constant, suggesting that there are residual fields in the plasma environment that maintain a nominal electron temperature long into the afterglow. The most likely source of this residual field is the ambipolar field (in the radial direction) that regulates charge loss to the walls. A simple estimate of this residual reduced field is  $kT_e \nabla n_e / (n_e N_g) \sim kT_e / (2rN_g) = 10$  Td (where  $kT_e$  is assumed to be 1 eV and  $r$  is 1 cm), comparable to the measured residual fields. This residual field sets a lower limit on the attainable values of E/N during the calibration process.

### ***IIIc Generation and detection of LCIF.***

The  $1s_5$  to  $3p_2$  state is excited by a  $<10$  ns laser pulse tuned to the transition centered at 394.9 nm. The laser pulse is generated from a laser-seeded, Q-switched Nd:YAG operating at 20 Hz (Powerlite 9020 DSL, Continuum). The third harmonic (355 nm) is used to pump an optical parametric oscillator/amplifier system (Sunlite OPO, Continuum) which converts the 355 nm laser light into conjugate signal and idler pairs. A grating incorporated into the cavity of the parametric oscillator produces laser linewidths on the order of  $0.1 \text{ cm}^{-1}$  or better. The amplified idler is centered at 789.8 nm and is doubled (FX-1, Continuum) to produce the desired 394.9 nm. The 394.9 nm laser beam is shaped into a 1 cm diameter beam using a beam expander constructed from a pair of plano-convex lenses. After expansion of the beam, the shaped beam is attenuated to  $\sim 1$  mJ/pulse and directed through the discharge. Laser induced fluorescence emanating from the  $3p_2$  to  $1s_2$  transition centered at 433 nm is monitored with a photomultiplier tube and is used to verify the tuning of the laser system.

Light emanating from the plasma chamber is collected with a lens and brought to an 0.5 meter imaging spectrometer (470 HR, Spex) via fiber optic cable. The output of the fiber is placed in close proximity to the entrance slit of the spectrometer (nominally set to  $200 \mu\text{m}$ ). The light is spectrally dispersed by a 1200 g/mm holographic grating and directed towards a gated, intensified-CCD (ICCD) camera (iStar, Andor) mounted at the exit port of the spectrometer. Nominal resolution of the spectrometer and camera system is  $\sim 0.02$  nm which yields a 20 nm wide window over the field of view of the ICCD sensor. The spectral dispersion of the imaging platform is obtained by using a series of noble gas pen lamps that have several lines in the spectral region captured by the ICCD camera while the relative spectral efficiency of the imaging platform is ascertained by a tungsten filament white light source operating at black body temperature of 3100 K. The spectral regions of interest identified in Table 1 are monitored by adjusting the position of the grating.

### ***IIId Procedure utilized for LCIF calibration***

Finally, having described the key elements utilized in generating and detecting LCIF, calibration of the diagnostic proceeds as follows. A set of the current limiting resistors are chosen to target a desired electron density range. The delay between the first voltage pulse and the second voltage pulse is fixed at 80  $\mu$ s to ensure that the electron energy associated with the first pulse has enough time to cool. For the chosen resistor set, combinations of the first and second voltage pulses are determined that yield either variable density at a fixed drift velocity or variable drift velocity at fixed densities. Measurements are then performed for the spectral windows of interest (Table 1) for each voltage combinations. The gating of the ICCD camera system is synchronized to both the firing of the laser and the operation of the plasma discharge through the use of digital delay generator (SRS 645). Typical gating of the intensified camera is for the duration of 150 ns which is initiated  $\sim$  10 ns after the 394.9 nm laser excites the  $1s_5$  atoms to prevent acquisition of any back scatter of the pump laser. Acquisition or integration time span tens of seconds or for hundreds of laser pulses for the LIF emanating from the  $3p_2$  state, up to 240 s for low intensity signals emanating from the higher collisional states. For a given measurement, both the total emission (consisting of both laser (collision) induced fluorescence and plasma induced emission) and the plasma emission without laser excitation are acquired. Emission generated from laser excitation is obtained by subtracting the plasma emission from the total emission. Three to five images are acquired to provide a measure of intensity fluctuation that can be caused by variations of the laser intensity or tuning. The images are then averaged together and individual lines (Section IVa) are extracted from the average images. Extraction consists of identifying line center of a desired transition and averaging over a  $\sim$  0.6 nm window ( $\pm$  15 pixels). The averaged intensities are then corrected for the imaging systems collection efficiency and acquisition time. As presented in Section IVb, the corrected intensities are then normalized to the LIF emanating from the  $3p_2$  state at 418 nm.

**IV. Calibration of the LCIF technique in Argon**

With the setup and procedure described in the previous section, calibrated LCIF trends are now discussed. In the following section, spectrally dispersed emission is presented with the intent of assessing which states are coupled to the laser excited state and the degree of spectral overlap or “contamination” that may be imposed on the targeted states of interest as outlined in Section II and presented in Table 1. Scaling trends of the LCIF are presented as functions of electron density and reduced electric field in Section IVb. These scaling trends are discussed in context of the predictions made by the two-state model in Section IIb and plotted in Figure 4.

***IVa Spectral dispersed emission generated by laser excitation***

Figure 8 illustrates characteristic emission emanating from the plasma ( $n_e=4.5 \times 10^{10}$  e/cm<sup>3</sup>,  $E/N=40$  Td,  $kT_{\text{Effective}}=4$  eV) after 394.9 nm laser excitation of the  $1s_5$  atoms to the  $3p_2$  state. The left hand column corresponds to background subtracted laser and laser-collision induced fluorescence generated by laser excitation while the right hand column corresponds to the (dark-count removed) plasma

induced emission. The vertical scales for the corresponding LIF (LCIF) and PIE spectra are kept constant for each spectral region of interest. The four lines emanating from the laser induced transition (Table 1) are the dominant lines in the 390 nm to 435 nm range (upper two plots of Figure 8). The lower intensity lines around 415 nm, 420 nm, 425 nm emanate from nearby 3p states. With the exception of the observed 425.9 nm line emanating from the  $3p_1$  state (0.05 eV above the  $3p_2$  state), these lines correspond to lower lying 3p states. Emission from these states is less than 10% of the LIF emanating from the laser excited state and is most likely generated by collisional processes as opposed to radiative processes and can be considered to be laser-collision induced fluorescence. Plasma induced emission in this spectral region mostly consists of the 415.9 nm and the 420.1 nm lines, both less than 10% of the LIF.

Laser-collision induced fluorescence and plasma induced emission emanating in the spectral region near 680 nm is presented in the third row of Figure 8. The two targeted LCIF lines at 675.3 nm and 687.1 nm correspond to the  $4d_3 \rightarrow 2p_{10}$  and  $4d_5 \rightarrow 2p_{10}$  transitions respectively and are the two most intense lines in this spectral region. Emission at 676.7 nm is observed in proximity of the 675.3 nm line and is  $\sim 5\%$  of the intensity of the 675.3 nm line. On the other hand, emission at 688.0 nm and 688.8 nm have intensities that become comparable to (8% and 25 % respectively) the nearby the 687.1 nm target. For the given plasma conditions, the plasma induced emission at 675.1 nm is about 30 percent of the intensity of the LCIF while the plasma induced emission at 687.1 nm is about one-half of the LCIF intensity.

Emission in the proximity of the targeted 641.6 nm line corresponding to the  $3s_5 \rightarrow 2p_{10}$  transition (0.15 eV above the laser-excited  $3p_2$  state) is presented in the fourth row of Figure 8. Several of the lines tabulated in Table 1 are observed in the LCIF spectrum, with the most intense line at 630.77 nm. Emission within a few nm of the 641.6 nm target line is observed to have ten percent or less of the 641.6 nm intensity. On the other hand, plasma induced emission at 641.6 nm is comparable to the LCIF observed at the same wavelength.

Finally, emission in the proximity of the target 591.2 nm line corresponding to the  $3s_5 \rightarrow 2p_{10}$  transition (0.316 eV above the laser excited  $3p_2$  state) is presented in the fifth row of Figure 8. Several lines are observed in that have intensities comparable to the targeted 591.2 nm line. These lines include the 586.0 nm line (0.335 eV above  $3p_2$ ), the 588.3 nm line (0.327 eV above  $3p_2$ ) and to a lesser extent, the 588.9 nm line (0.498 eV above  $3p_2$ ). Additional lines are observed that have intensities that are roughly 10% or less of the intensity of the targeted 591.2 nm line. Plasma induced emission in this spectral region consists of the 588.9 nm and the 591.2 nm lines, both of which are comparable in magnitude to the LCIF.

#### ***IVb Scaling trends of emitted light from targeted LCIF transitions***

The scaling trends for both the targeted LCIF transitions as well as the neighboring or nearby lines are presented in Figure 9. All of the LCIF transitions are normalized to the measured 418.2 nm LIF emanating from the laser excited  $3p_2$  state. The left column contains the observed LCIF as a function of

electron density at a reduced electric field ( $E/N$ ) of 28 Td while the right column contains the observed LCIF as a function of reduced electric field at an electron density of  $4.5 \times 10^{10} \text{ e/cm}^3$ . The upper row of plots correspond to observed LCIF trends with wavelengths near 680 nm, the middle row of plots correspond to observed LCIF trends with wavelengths near 640 nm and the lower row of plots correspond to observed LCIF trends with wavelengths near 590 nm. The dashed lines are added to aide in illustrating the scaling of the LCIF with either electron density or reduced electric field. Scaling trends of the LIF emanating from the  $3p_2$  state are not shown as the normalized LIF does not depend on either electron density or reduced electric field in the weakly absorbing plasma interrogated in this study. The relative LIF from the  $3p_2$  state emitted from the plasma may change as the plasma becomes optically thick as the light from the various  $3p_2$  transitions have different absorption mean free paths.

### *LCIF scaling with electron density*

Scaling trends of the LCIF are plotted as functions of the electron density in the left column of Figure 9. The electron drift velocities were nominally  $3 \times 10^6 \text{ cm/s}$  which corresponds to a reduced electric field of 28 Td. Variation in the drift velocities and reduced electric fields were  $\sim 5\%$ . The electron density dependence of the 687.1 nm line, emanating from the  $4d_5$  state, ( $\Delta E = 0.024 \text{ eV}$ ) demonstrates a linear scaling for electron densities exceeding  $2 \times 10^{10} \text{ e/cm}^3$ . Below this value, the relative LCIF signal plateaus. Similarly, the 675.3 nm line, emanating from the  $4d_3$  state ( $\Delta E = 0.055 \text{ eV}$ ) scales linear with electron densities above  $5 \times 10^{10} \text{ e/cm}^3$ . By contrast, LCIF at 688.8 nm, emanating from the  $4s''_1$  state ( $\Delta E = 0.265 \text{ eV}$ ) demonstrates a linear scaling over the full range of investigated electron densities. Similar linear scaling with electron density is observed for the LCIF emanating from the higher lying states that are presented in the middle and lower plots of Figure 9. Deviations of these signals from the linear scaling trend likely stem from minor variations in the reduced electric field.

As discussed in the two-state model presented in Section IIb, the scaling of the LCIF is anticipated to be linear with electron density (black curve, Figure 4a) until competing mechanisms become comparable to the electron driven population redistribution. In the low electron-density limit one such competing mechanism is neutral species-induced redistribution which depends on both the density of neutral atoms as well as the energy gap between the laser-excited state and collisionl-populated state. For the two transitions emanating from the energetically nearby  $4d_2$  and  $4d_5$  states, the energy gap is comparable to the average energy a room temperature argon atom possesses ( $kT_g \sim 0.025 \text{ eV}$  at 300 K). For an argon pressure of 100 mTorr ( $N_g \sim 3.5 \times 10^{15} \text{ Atoms/cm}^3$ ) and using a neutral induced collisional rate coefficient of  $K_g = 1.4 \times 10^{-10} \text{ cm}^3/\text{s}$  the neutral collision rate ( $K_g N_g$ ) is  $5 \times 10^5 \text{ s}^{-1}$  is equal to the electron collision rate of  $5 \times 10^5 \text{ s}^{-1}$  for an electron density of  $5 \times 10^{10} \text{ e/cm}^3$ , assuming an electron induced collisional rate coefficient of  $K_e = 1 \times 10^{-5} \text{ cm}^3/\text{s}$  (Figure 2). The LCIF emanating from the lower lying  $4d_5$  state (687.1 nm) is more influenced by the neutral argon atoms than the higher  $4d_2$  state (675.3 nm) is. This is illustrated by the location of the knee in LCIF curves (transition from linear scaling to flat) as well as the magnitude of base line LCIF signal observed at lower electron densities. The linear scaling of the LCIF to lower densities is anticipated to reestablish at lower pressures.

On the other hand, when the energy gap between the laser excited state and the collision-populated state increases to a value considerably greater than the average energy of an argon atom, the contribution to the LCIF signal by the neutral atoms is significantly reduced. For example, when the energy gap is increased to 0.152 eV as is the case for the  $3s_5$  state that produces the 641.63 nm LCIF (middle plot in the left column) the neutral atom collision rate constant is reduced by a factor of  $\sim 10^{-3}$  ( $e^{-0.152/0.022}$ ). Again assuming an electron induced collisional rate coefficient of  $K_e=10^{-5}$  cm<sup>3</sup>/s (Figure 2), the neutral induced contribution of the LCIF becomes comparable to the electron induced contribution of the LCIF at electron densities of  $\sim 5 \times 10^7$  e/cm<sup>3</sup> (at 100 mTorr).

Finally, within the limits of the variation in the obtained data, the LCIF trends do not appear to deviate from linear scaling at the higher limit of densities interrogated in this study as was predicted by the two state model for increasing excitation (electron or neutral induced) out of the LCIF emitting state (Figure 4a). This observation implies that radiative relaxation from the LCIF emitting state is still the dominant loss mechanism under the investigated conditions.

#### *LCIF scaling with reduced electric field*

Scaling trends of the LCIF are plotted as functions of the reduced electric field in the right column of Figure 9. The plasma density was nominally  $4.5 \times 10^{10}$  e/cm<sup>3</sup> but varied by as much as  $\sim \pm 10$  %. LCIF emitted from the lowest lying  $4d_5$  (687.1 nm) and  $4d_2$  (675.3 nm) states is observed to be independent of the reduced electric field. On the other hand, the LCIF emitted from the higher lying  $4s''_1$  state (688.9 nm) exhibits a non-linear but monotonically increasing dependence on the reduced electric field. At lower values of the reduced electric field (1 Td to  $\sim 5$  Td) the 688.9 nm LCIF is essentially flat. For modest values of the reduced electric field (5 Td to 20 Td) the 688.9 nm LCIF is a super-linear function of the reduced electric field (slope of the blue dashed line is greater than unity on the log-log plot). At higher values ( $>20$  Td), the 688.9 nm LCIF tends to level off. Similar functional dependence on the reduced electric field is observed for the other LCIF signals generated from higher lying states (lower two plots, right column of Figure 9). In all instances, there is a persistent baseline that spans the 1 Td to 5 Td range. Above 5 Td, the LCIF signals demonstrate strong dependence on the reduced field until 20 Td. Above 20 Td, the LCIF signals tend to level off with increasing E/N.

Predicted scaling of the temperature dependence of the LCIF by the two-state model is presented in Figure 4b. The predicted trends, while only qualitative at best, indicate that LCIF is essentially independent of electron temperature (regulated by E/N) when the energy gap between the laser excited state and the collision-populated state is considerably less than the electron temperature. This temperature-independent behavior is observed in the 687.1 nm and 675.3 nm LCIF signals (upper right plot) over the entire range of E/N interrogated. Furthermore, this (nearly) temperature-independent behavior is observed in all LCIF trends for values of reduced fields greater than 20 Td. On the other hand, when the electron temperature is comparable to or less than the energy gap between the laser excited state and the collision-populated state there is a strong (super-linear) dependence of the predicted LCIF on the electron temperature. This strong dependence of LCIF on the reduced electric



field is observed for the higher lying states emitting 688.1 nm (upper right plot), 630.8 nm (middle right plot) and 588.6 nm (lower right plot).

Not predicted by the simple two-state model is the low-energy baseline that is observed in the measured LCIF. As discussed in Section IIIb, there is a residual effective electric field that persists in the plasma long into the afterglow. Estimates of this residual field were comparable to ambipolar fields that are established to regulate charge loss to the glass tube. It is anticipated (though to be confirmed) that the intensity of the LCIF originating from the higher lying states will continue to be functions of E/N at lower values of E/N.

### *Combined LCIF ratios*

Scaling trends of the summed or combined LCIF emanating near 641 nm and 589 nm are presented in Figure 10 as functions of E/N. For the 641 nm case, the sum consists of contributions by the 641.3 nm and 643.6 nm lines while for the 589 nm case, the sum consists of contributions by the 586 nm, 588.26 nm, 588.6 nm and 591.2 nm lines. Furthermore, both summed lines are normalized not to the LIF emanating from the 3p<sub>2</sub> state but the LCIF emanating from the 4d<sub>3</sub> state at 675.28 nm. The LCIF is scaled in this manner for two reasons. First, implementation of the LCIF technique for two-dimensional imaging utilizes narrow-band interference filters (bandwidth ~ 5 nm) centered on the lines of interest. Therefore, the imaged light will consist of contributions from the listed lines. More importantly however, ratios of LCIF emanating from states that have different energy-dependent population rates provides a handy way to factor out the electron-density dependent contribution of the LCIF. As the LCIF from both states are proportional to n<sub>e</sub>\*K<sub>e</sub>, then it follows that the ratio of LCIF can be approximated as

$$\frac{LCIF_u}{LCIF_l} \propto \frac{n_e A_u K_{e,u}}{n_e A_l K_{e,l}} \propto \frac{A_u K_{e,u}}{A_l K_{e,l}}, \quad (7)$$

where the subscripts *u* and *l* correspond to upper and lower states respectively. By neglecting (or removing) non-electron induced coupling into either state the LCIF signals depend on the electron density alone. As a result, the ratio of the two signals becomes independent of electron density. Instead, the ratio of the two LCIF signals now depends on the relative functional dependence of the collision rates K<sub>e</sub>(E/N). For the limiting case where the LCIF from one of the states is independent of E/N, as is the case for LCIF emanating from the lower-lying 4d states, the ratio is a direct measure of excitation rate.

### **V. Demonstration of the 2D-Planar LCIF technique**

Finally, the application of the LCIF method to the mapping of electron densities and reduced electric field is demonstrated in a structurally “interesting” argon discharge. The demonstration configuration is portrayed in Figure 11 and consists of an aluminum disc electrode with embedded samarium cobalt magnets. The central cylindrical magnet is 6.35 mm in diameter and 6.35 mm thick. The outer ring magnet has an outer diameter of 25.5 mm, an inner diameter of 15.7 mm, and is 6.35 mm thick. The poles of both magnets are oriented along their axis and arranged in opposite directions

so as to form a “closed” magnetic loop structure. The peak magnetic field at the surface of the electrode is about 1.2 kG. Simulations of the magnetic field, along with vector components of the field are depicted above the electrode in Figure 11. A seed plasma is generated in 10 mTorr of argon by a pulse modulated RF voltage applied to capacitively coupled electrode (not shown) above the aluminum disc. The RF frequency is 10 MHz, and the modulation frequency is 20 Hz (synchronized to the 20 Hz laser). The on time of the RF power is 1 ms (2 % duty cycle). A pulsed bias (-1000 volt amplitude, 5  $\mu$ s long) is applied to the magnetized electrode 30  $\mu$ s into the afterglow of the RF plasma. The generation and acquisition of LIF and LCIF occur  $\sim$  1  $\mu$ s after the -1000 Volt bias is applied.

The laser beam is formed into a planar sheet 20 mm high by  $\sim$  1 mm thick and directed through the vacuum vessel containing the magnetized electrode. Care is taken to reduce clipping of the electrode by the laser beam. LIF is generated by excitation of the  $1s_5$  to  $3p_2$  transition (394.5 nm) while LIF and LCIF are monitored by the gated intensified CCD camera filtered with narrow band ( $\sim$  5 nm) interference filters centered on transitions emanating from the  $3p_2$  state (418 nm),  $4d_3$  state (675 nm) and the  $4s'_1$  state (590 nm). 10 ns after laser excitation is complete, the ICCD camera is gated for a duration of 150 ns. Accumulation times span a range from 20 s (LIF at 418 nm) to 120 s (LCIF at 590 nm) and several images ( $\sim$  20) are acquired and averaged.

Images of the observed plasma induced emission, laser (collision) induced fluorescence and resulting maps of the  $1s_5$  metastable density, electron density and E/N are presented in Figure 13. As indicated by the plasma induced emission taken at the three different wavelengths, much of the excitation and ionization occurs in the vicinity of the magnetized electrode. It is expected (though not confirmed) that this excitation occurs in the region where the magnetic field is expected to contain a strong horizontal component (parallel to the electrode). The high field should offer considerable impedance to the electron flow. The localization of excitation is further supported by the observed structure in the observed LIF at 418 nm that serves as measure of the  $1s_5$  metastable distribution.

The spatial distribution of electrons (obtained by taking the ratio of the 675 nm LCIF to the 418 nm LIF) in response to the pulsed bias applied cathode is quite complex. In the center of the electrode, where the magnetic field is mostly perpendicular to the electrode, the electrons can travel parallel to the magnetic field and easily flow away from the electrode. On the other hand, in the region between the two magnets, the magnetic field is parallel to the electrode and the electrons are trapped by the strong magnetic field and cannot react to the applied field. The confined electrons likely experience a strong  $E \times B$  drift as indicated by the large electron densities present in this region. The ratio of 590 nm LCIF to the 675 nm LCIF which provides a direct measure of  $v_{\text{Drift}}$  and which is subsequently used to infer E/N confirms the presence of a high energy region in the vicinity of the electrode where excitation of PIE and generation of metastable atoms were observed. Comparable ring-like structure of have been observed in high power impulse magnetron sputtering (HiPIMS) devices<sup>53 54 55 56</sup>. While further investigation of this structure is beyond the scope of the demonstration, these images illustrate the ability of the LCIF method to access this challenging environment.

VI. Conclusions

In this study, the calibration and demonstration of the LCIF technique applied to argon plasma discharges is discussed. It is demonstrated that LCIF emanates from several states that are energetically above the laser excited  $3p_2$  state and that the intensity of the LCIF scales with both electron density as well as the reduced electric field (which can also serve as a measure of electron energy). At lower electron density limits, it was demonstrated that the  $4s_3$  and  $4s_5$  states (energetically close to the laser excited  $3p_2$ ) were subject to collisional population by background neutrals. This coupling reduces the energy gap between the laser-excited state and the state emanating the LCIF. It is also demonstrated that the E/N dependence of the coupling between two states likewise depends on the energy spacing between the coupled states. Therefore, by properly selecting laser excited and monitoring appropriate collisional populated states, measures of the electron density and E/N can be obtained. Finally, application of the LCIF technique to structurally interesting plasma demonstrates the ability of the diagnostic technique to interrogate challenging plasma environments.

VII. Acknowledgements

This work was supported by the Office of Fusion Energy Science at the U.S. Department of Energy under contracts DE-AC04-94SL85000 and DE-SC0001939.

References

<sup>1</sup> M. A. Lieberman, J. P. Booth, P. Chabert, J. M. Rax and M. M. Turner, Plasma Sources Sci. and Technol. **11**, 283 (2002).  
<sup>2</sup> P. Chabert, J. L. Raimbault, J. M. Rax and M. A. Lieberman, Phys. Plasma **11**, 1775 (2004).  
<sup>3</sup> A. Perret, P. Chabert, J. P. Booth, J. Jolly, J. Guillon, P. Auvray, App. Phys. Lett. **83**, 243 (2003).  
<sup>4</sup> G. A. Hebner, E. V. Barnat, P. A. Miller, A. M. Paterson and J. P. Holland, Plasma Sources Sci. and Technol. **15**, 879 (2006).  
<sup>5</sup> P. A. Miller, E. V. Barnat, G. A. Hebner, A. M. Paterson and J. P. Holland, Plasma Sources Sci. and Technol. **15**, 889 (2006).  
<sup>6</sup> E. V. Barnat, P. A. Miller, G. A. Hebner, A. M. Paterson, T. Panagopoulos, E. Hammond and J. P. Holland, Applied Phys. Lett. **90**, 201503 (2007).  
<sup>7</sup> C. G. N. Lee, K. J. Kanarik and R. A. Gottscho, J. Phys. D: Appl. Phys. **47**, 273001 (2014).  
<sup>8</sup> J. Schulze, E. Schungel, Z. Donko, D. Luggenholscher and U. Czarnetzki, J. Phys. D: Appl. Phys. **43**, 124016 (2010).  
<sup>9</sup> X.M. Zhu, Y. K. Pu, Y. Celik, S. Siepa, E. Schungel, D. Luggenholscher and U. Czarnetzki, Plasma Sources Sci. and Technol. **21**, 024003 (2012).  
<sup>10</sup> G. A. Hebner, J Appl. Phys. **80**, 2624 (1996).  
<sup>11</sup> J. Ropcke, G. Lombardi, A. Rousseau and P. B. Davies, Plasma Sources Sci. and Technol. **15**, s148 (2006).

- <sup>12</sup> L. J. Overzet and M.B. Hopkins, J. Appl. Phys. **74**, 4323 (1993).
- <sup>13</sup> B.K. McMillin and M.R. Zachariah, J. Appl. Phys. **77**, 5538 (1995).
- <sup>14</sup> K. L. Steffens and K. A. Sobolewski, J. Vac. Sci. Technol. A **17**, 517 (1999).
- <sup>15</sup> E. V. Barnat, P. A. Miller and A. M. Paterson, Plasma Sources. Sci. Technol. **17**, 045005 (2008).
- <sup>16</sup> E. V. Barnat and V. I. Kolobov, Appl. Phys. Lett. **102**, 034104 (2013).
- <sup>17</sup> E. V. Barnat and K. Frederickson, Plasma Sources Sci. and Technol. **19**, 055015 (2010).
- <sup>18</sup> A. A. Hubble, E. V. Barnat, B.R. Weatherford and J. E. Foster, , Plasma Sources Sci. and Technol. **23**, 055030 (2014).
- <sup>19</sup> B. R. Weatherford, Z. Xiong, E. V. Barnat and M. J. Kushner, J. Appl. Phys. **116**, 103305 (2014).
- <sup>20</sup> U. Czarnetzki, D. Luggenholscher, H. F. Dobebe, Phys. Rev. Lett. **81**, 4592 (1998).
- <sup>21</sup> U. Czarnetzki, D. Luggenholscher, H. F. Dobebe, Plasma Sources. Sci. Technol. **8**, 230 (1999).
- <sup>22</sup> E. Wagenaars, G.M.W. Krossen and M. D. Bowden, Phys. Rev. A, **74**, 033409 (2006).
- <sup>23</sup> T. Jiang, M. D. Bowden, E. Wagenaars, E. Stoffels, and G.M.W. Krosen, New J. of Phys **8**, 202 (2006).
- <sup>24</sup> E. V. Barnat and G. A. Hebner, Appl. Phys.Lett. **85**, 3393 (2004).
- <sup>25</sup> E. V. Barnat, Plasma Sources Sci. and Technol. **20**, 053001 (2011).
- <sup>26</sup> I. S. Borthwick, A. M. Paterson, D. J. Smith and R. S. Stewart, J. Phys. B: At. Mol. Opt. Phys. **33**, 4513 (2000).
- <sup>27</sup> A. M. Paterson, D. J. Smith, I. S. Borthwick and R. S. Stewart, J. Phys. B: At. Mol. Opt. Phys. **34**, 1815 (2001).
- <sup>28</sup> R. S. Stewart, D. J. Smith, I. S. Borthwick and A. M. Paterson, Phys. Rev. E **62**, 2678 (2000).
- <sup>29</sup> R. S. Stewart, D. J. Smith, J. Phys. D: Appl. Phys. **35**, 1777 (2002).
- <sup>30</sup> C. F. Burrell and H.-J. Kunze, Phys. Rev. A **18**, 2081 (1978).
- <sup>31</sup> B. Dubreuil and P. Prigent, J. Phys. B: At. Mol. Opt. Phys. **18**, 4597 (1985).
- <sup>32</sup> K. Tsuchida, S. Miyake, K. Kadota and J. Fujita, Plasma Physics **25**, 991 (1983).
- <sup>33</sup> E. A. Den Hartog, T. R. O'Brian and J. E. Lawler, Phys. Rev. Lett. **62**, 1500 (1989).
- <sup>34</sup> K. Dzierzega, K. Musiol, E. C. Benck and J. R. Roberts, J. Appl. Phys. **80**, 3196 (1996).
- <sup>35</sup> M. Krychowiak, Ph Mertens, R. Konig, B. Schweer, S. Brezinsek, O. Schmitz, M. Brix, U. Samm and T. Klinger, Plasma Phys. Control. Fusion **50**, 65015 (2008).
- <sup>36</sup> Nersisyan, T. Morrow, and W. G. Graham, Appl. Phys. Lett. **85**, 1487 (2004)
- <sup>37</sup> T. D. Nguyen and N. Sadeghi, Phys. Rev. A **18**, 1388 (1978).
- <sup>38</sup> G. Inoue, D. W. Setser and N. Sadeghi, J. Chem. Phys. **76**, 977 (1982).
- <sup>39</sup> J. M. Palomares, W. A. A. D. Graef, S. Hubner and J. J. A. M. van der Mullen, Spectrochimica Acta B **88**, 156 (2013).
- <sup>40</sup> E. A. D. Carbone, S. Hubner, J. J. A. M. van der Mullen, G. M. W. Krosen and N. Sadeghi, J. Phys. D: Appl. Phys. **46**, 415202 (2013).
- <sup>41</sup> A. Bogaerts, R. Gijbels and J. Vlcek, J. Appl. Phys. **84**, 121 (1998).
- <sup>42</sup> A. Yanguas-Gil, J. Cotrion and L. L. Alves, J. Phys. D:Appl. Phys. **38**, 1588 (2005).
- <sup>43</sup> W. L. Wiese, M. W. Smith, and B. M. Glennon, *Atomic Transition Probabilities 4/V1* (Nat. Stand. Ref. Data. Ser., Nat. Bur. Stand. Washington DC, 1966).
- <sup>44</sup> G.J.M. Hagelaar and L.C. Pitchford, Plasma Sources Sci. and Technol. **14**, 722 (2005).
- <sup>45</sup> BOLSIG+ solver, [www.lxcat.net](http://www.lxcat.net), retrieved March 16, 2015.
- <sup>46</sup> IST-Lisbon database, [www.lxcat.net](http://www.lxcat.net), retrieved March 16, 2015.
- <sup>47</sup> S. J. Buchsbaum and S. C. Brown, Phys. Rev. **106**, 196 (1957).
- <sup>48</sup> A. G. Robertson, Aust. J. Phys. **30**, 39 (1977).
- <sup>49</sup> Y. Nakamura and M. Kurachi, J. Phys. D: Appl. Phys. **21**, 718 (1988).
- <sup>50</sup> J. L. Pack, R. E. Voshall, A. V. Phelps and L. E. Kline, J. Appl. Phys. **71** 5363 (1991).
- <sup>51</sup> D. A. Dahl, T. H. Teich, C. M. Franck, J. Phys. D: Appl. Phys. **45**, 485201 (2012).
- <sup>52</sup> Lieberman, M., and A. Lichtenberg, John Wiley & Sons, Chapter 5, (2005).
- <sup>53</sup> A. Anders, P. Ni, and A. Rauch, J. Appl. Phys., vol. 111, p. 053304, (2012).
- <sup>54</sup> J. T. Gudmundsson, N. Brenning, D. Lundin, and U. Helmersson, J. Vac. Sci. Technol. A, vol. 30, p. 030801, (2012).
- <sup>55</sup> A. P. Ehasarian, A. Hecimovic, T. de los Arcos, R. New, V. Schulz-von der Gathen, M. Böke, and J. Winter, Appl. Phys. Lett., vol. 100, p. 114101, (2012).
- <sup>56</sup> J. Andersson, P. Ni, and A. Anders, Appl. Phys. Lett., vol. 103, p. 054104, (2013).

**Figure Captions**

Figure 1. Illustration of key transitions in the argon manifold utilized for the implementation of the laser-collision induced fluorescence (LCIF) method described in this study. Laser excitation occurs from the  $1s_5$  into the  $3p_2$  state. Collision induced fluorescence is monitored from nearby but energetically uphill states.

Figure 2. (a) Electron energy dependence of excitation cross-sections and (b) electron temperature dependence of excitation rates coupling the laser excited  $3p_2$  state to representative higher lying states that produce LCIF. Functional forms of the cross-sections plotted in (a) are described in the text and are used to compute the rates in (b).

Figure 3. Illustration of the computed time dependent evolution of the (a) laser induced fluorescence from the laser excited state  $3p_2$  state and the (b) the collision induced fluorescence emanating from the  $4d_3$  state for three different electron densities. For these calculations, the neutral collisions are ignored while the electron temperature is 1 eV.

Figure 4. (a) Predicted scaling of the normalized laser-collision induced fluorescence as a function of the electron density. The blue dashed lines illustrate the role increased neutral collisions have on the low density detection limit while the red dashed lines illustrate the role increased excitation from the collisionally populated state has on the upper density limit. (b) Predicted scaling of the normalized laser-collision induced fluorescence as a function of reduced electric field ( $E/N$ ) and effective electron temperature. The various lines refer to states that have increasing  $\Delta E_{\text{Gap}}$  above the laser excited state as discussed in Section II and used in Eq. 3.

Figure 5. (a) Illustration of the discharge chamber, including associated diagnostics utilized to interrogate the key plasma parameters of the discharge. (b) Representative temporal evolution of the electron density (upper plots) and discharge current observed in the double pulsed plasma utilized in calibrating the LCIF technique. The heating voltage pulse is highlighted in the shaded box and the plots on the left indicate the time that laser based measurements are performed with respect to the heating voltage pulse.

Figure 6. Scaling trends of (a) the current densities, (b) the changes in both the excited state species ( $n_m$ ) and the electron densities ( $n_e$ ), (c) the induced drift velocity ( $v_D$ ) and collision frequency ( $\nu_c$ ) and (d) the reduced electric field ( $E/N$ ) as functions of the applied heating voltage ( $V_{\text{Heating}}$ ).

Figure 7. (a) Comparison of ionization rates to diffusiional losses and (b) collision frequencies as functions of reduced electric field ( $E/N$ ) and effective electron temperature. These curves are utilized to benchmark measured  $E/N$  values to observed trends in electron densities with applied heating voltage (Figure 6).

Figure 8. (Left column) Measured laser induced fluorescence (LIF) and laser-collision induced fluorescence (LCIF) and (Right column) measured plasma induced emission (PIE). Measurements are performed over the spectral regions of interest presented in (Table 1). The measurements are performed in a 100 mTorr argon plasma that has an electron density of  $4.5 \times 10^{10} \text{ e/cm}^3$  and an effective electron temperature of 4 eV.

Figure 9. (a) Key scaling trends of target LCIF signals (normalized to LIF from  $3p_2$ ) as functions of electron density. The E/N and effective electron temperature are nominally kept constant at a value of 28 Td and 3.9 eV. (b) Key scaling trends of target LCIF signals (normalized to LIF from  $3p_2$ ) as functions of reduced electric field (E/N). The electron density is nominally kept constant at a value of  $4.5 \times 10^{10} \text{ e/cm}^3$ . Both data sets are acquired in a 100 mTorr argon discharge. Dashed lines are used to convey power-law scaling of the observed signals.

Figure 10. Ratio of E/N sensitive LCIF signals to E/N insensitive LCIF signal (675.2 nm) as functions of E/N. Data used to assemble this plot is obtained from Figure 9b. Dashed lines are used to convey power-law scaling of the observed signals.

Figure 11. Illustration of magnetized electrode and voltage waveform used to generate the structured plasma. Both the magnitude and vector components of magnetic field are illustrated in the region above the electrode.

Figure 12 Measured plasma induced emission (upper row), LIF or LCIF (middle row) and analyzed properties of the plasma discharge 1  $\mu\text{s}$  after the magnetized electrode is biased from  $\sim 0$  Volts to -1000 Volts.

### Table Captions

Table 1. List of target states used to generate LIF or LCIF after laser excitation from the  $1s_5$  state to  $3p_2$  state.

Target transitions	Wavelength (nm)	A (x10 <sup>6</sup> s <sup>-1</sup> )	ΔE (eV)	Notes
<b>1s<sub>5</sub> -&gt; 3p<sub>2</sub></b>	<b>394.9</b>	<b>0.46</b>	<b>0</b>	<b>Laser excitation transition</b>
3p <sub>2</sub> -> 1s <sub>4</sub>	404.6	0.04	0	Coupled but weak
3p <sub>2</sub> -> 1s <sub>3</sub>	418.2	0.56	0	Strongest line, potential contamination
3p <sub>2</sub> -> 1s <sub>2</sub>	433.5	0.39	0	Well isolated, but not strong
<b>4d<sub>5</sub>-&gt;2p<sub>10</sub></b>	<b>687.13</b>	<b>2.8</b>	<b>0.024</b>	<b>Target LCIF - very close to pumped state</b>
4s <sub>1</sub> <sup>'''</sup> ->2p <sub>7</sub>	688.82	0.25	0.265	Observed line close to LCIF
4s <sub>1</sub> <sup>''</sup> ->2p <sub>7</sub>	687.96	0.18	0.268	Observed line close to LCIF
<b>4d<sub>3</sub>-&gt;2p<sub>10</sub></b>	<b>675.28</b>	<b>1.9</b>	<b>0.055</b>	<b>Target LCIF - close to pumped state</b>
4s <sub>1</sub> <sup>'</sup> ->2p <sub>6</sub>	676.66	0.4	0.316	Observed line close to LCIF
<b>3s<sub>5</sub>-&gt;2p<sub>10</sub></b>	<b>641.63</b>	<b>1.2</b>	<b>0.152</b>	<b>Target LCIF -</b>
3s <sub>4</sub> ->2p <sub>10</sub>	638.47	0.42	0.161	Observed line close to LCIF
3s <sub>2</sub> ->2p <sub>8</sub>	643.16	0.05	0.335	Observed line close to LCIF
5d <sub>3</sub> ->2p <sub>6</sub>	630.77	0.60	0.450	Observed line close to LCIF
5d <sub>6</sub> ->2p <sub>7</sub>	636.49	0.56	0.413	Observed line close to LCIF
5d <sub>5</sub> ->2p <sub>6</sub>	636.96	0.42	0.431	Observed line close to LCIF
3s <sub>4</sub> ->2p <sub>10</sub>	638.47	0.42	0.161	Observed line close to LCIF
<b>4s<sub>1</sub><sup>'</sup>-&gt;2p<sub>10</sub></b>	<b>591.21</b>	<b>1.05</b>	<b>0.316</b>	<b>Target LCIF</b>
3s <sub>3</sub> ->2p <sub>10</sub>	588.26	1.2	0.327	Observed line close to LCIF
3s <sub>2</sub> ->2p <sub>10</sub>	586.03	0.29	0.335	Observed line close to LCIF
4s <sub>5</sub> ->2p <sub>9</sub>	588.86	1.29	0.494	Observed line close to LCIF
4s <sub>4</sub> ->2p <sub>8</sub>	592.8812	1.10	0.498	Observed line close to LCIF
5s <sub>1</sub> <sup>''</sup> ->2p <sub>6</sub>	583.42	0.52	0.609	Observed line close to LCIF
4s <sub>3</sub> ->2p <sub>4</sub>	597.1601	1.10	0.671	Observed line close to LCIF

Table 1

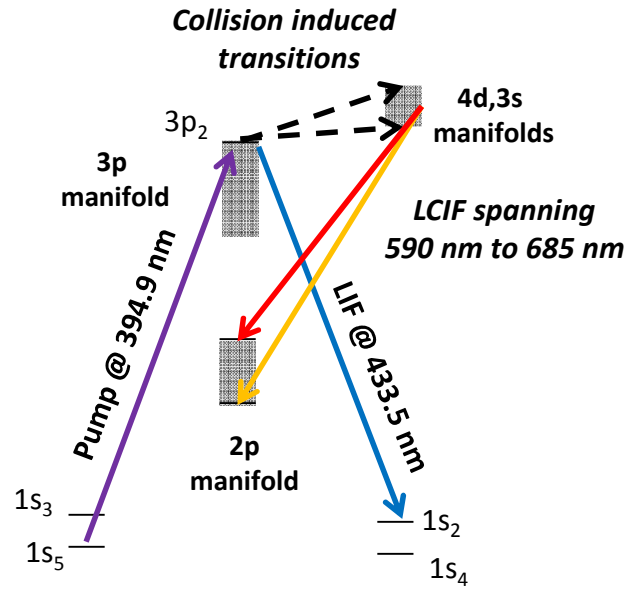


Figure 1



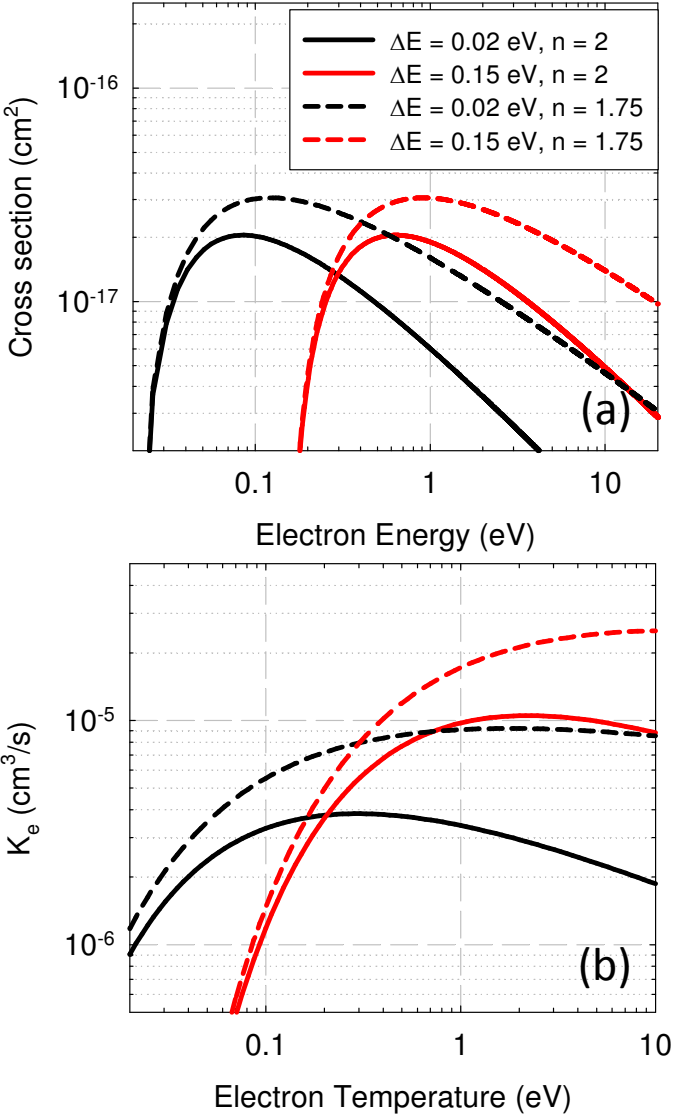


Figure 2

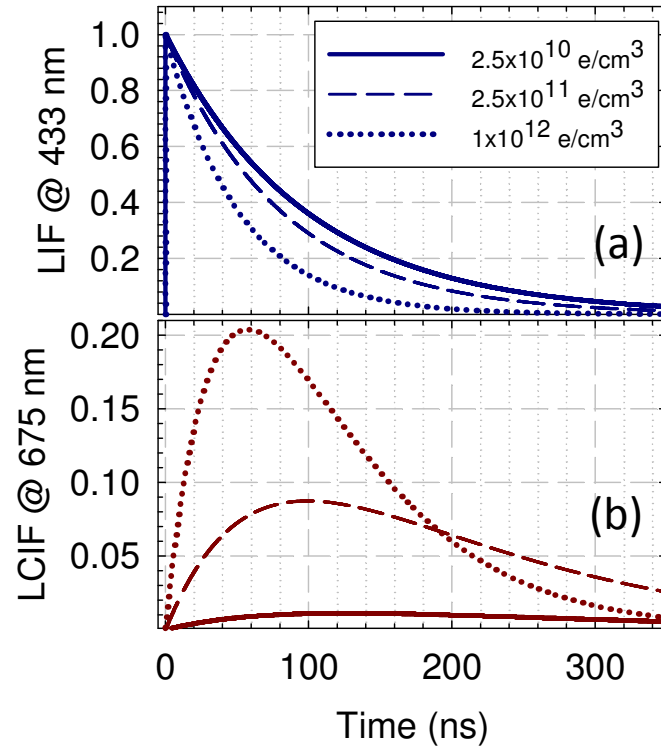


Figure 3

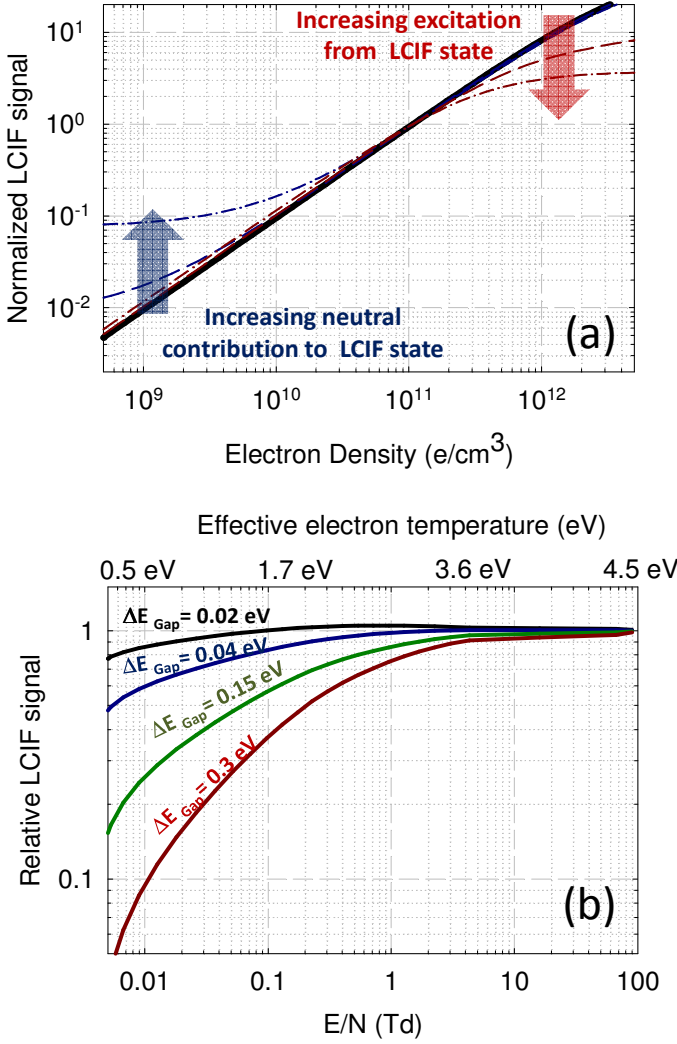


Figure 4

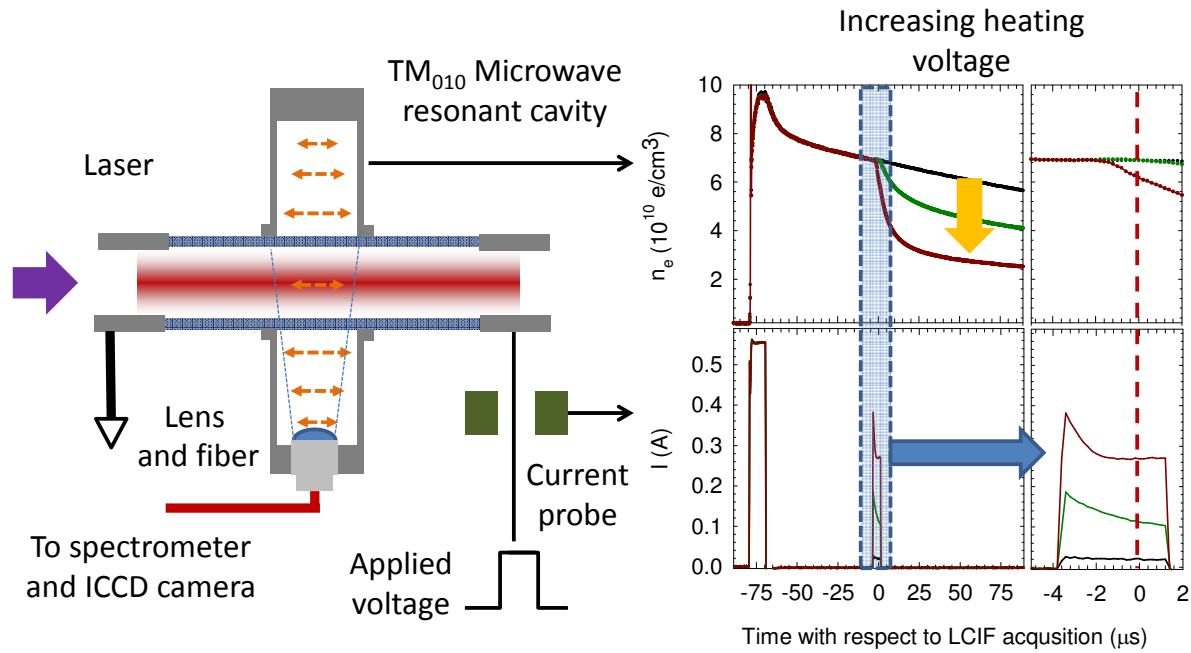


Figure 5

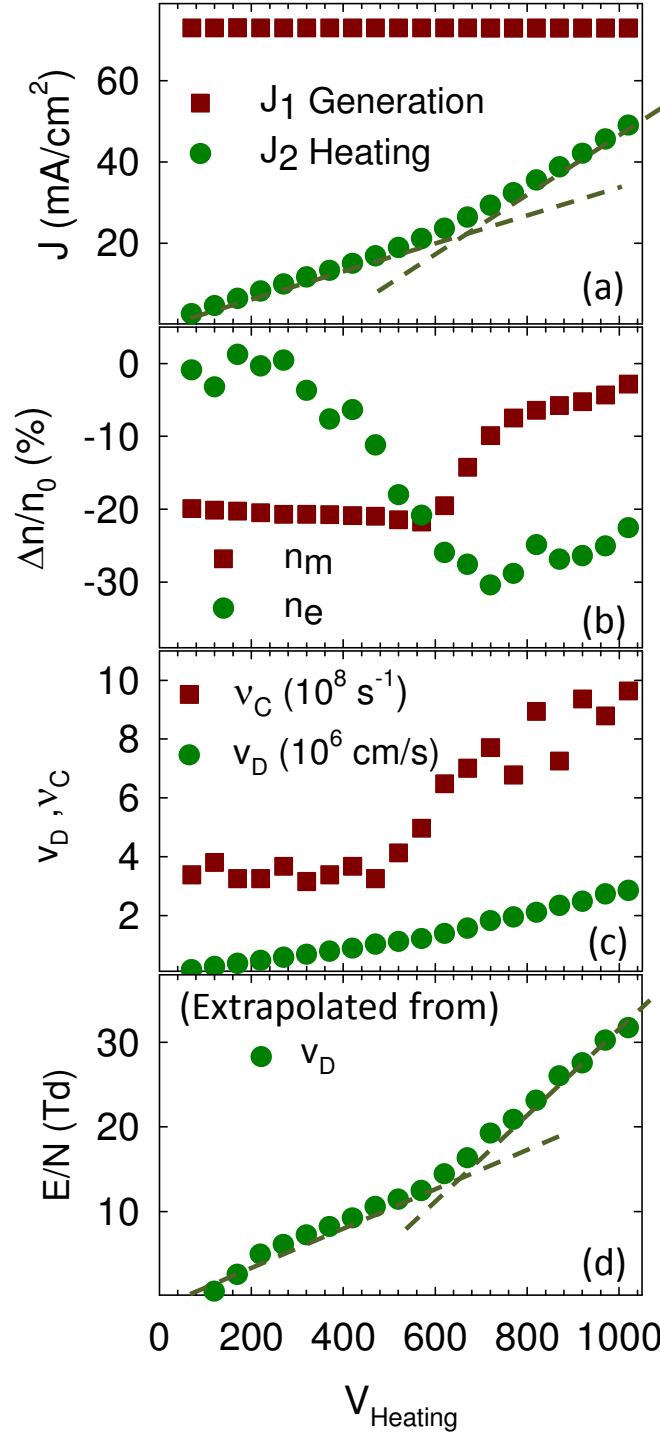


Figure 6

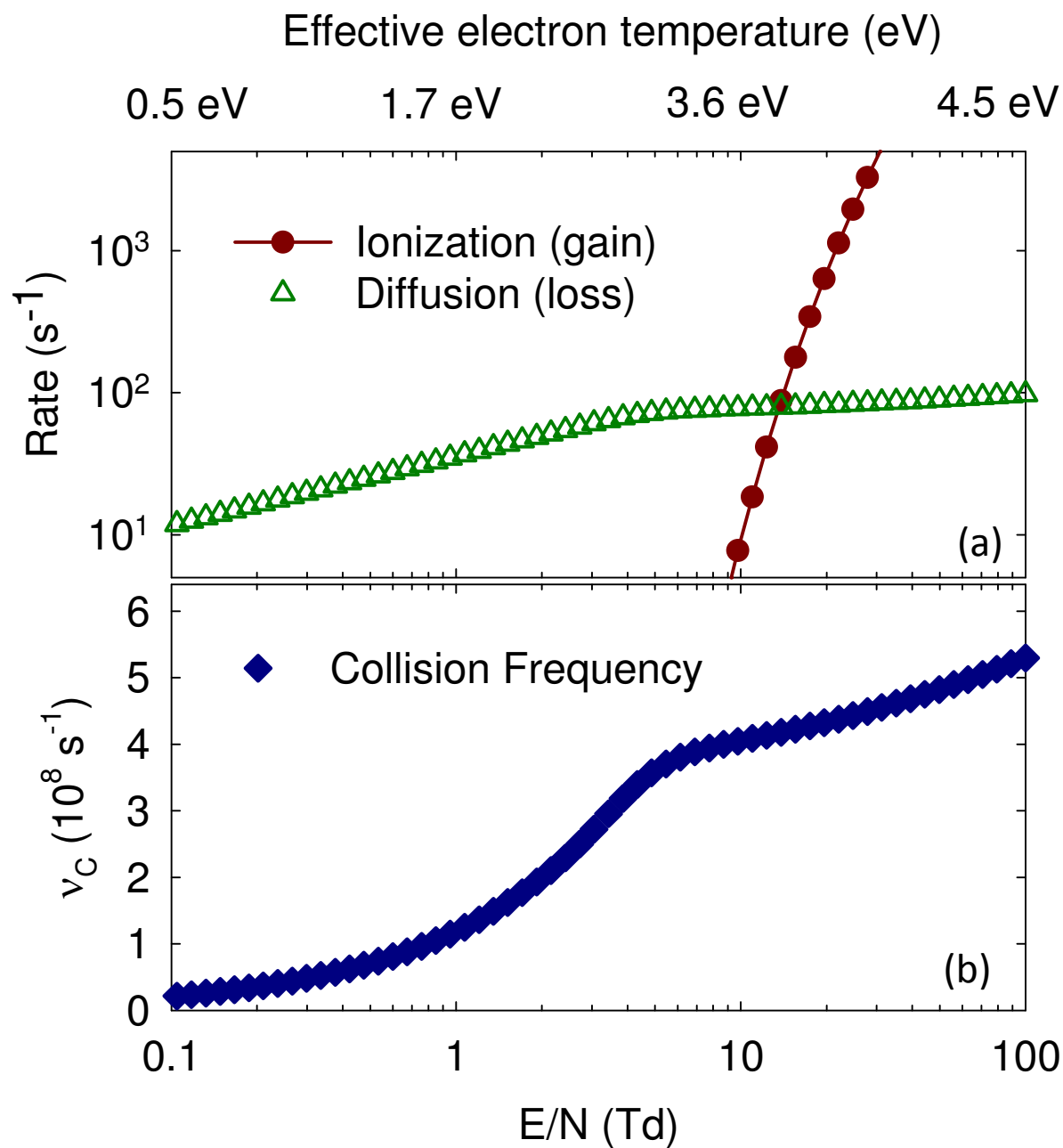


Figure 7

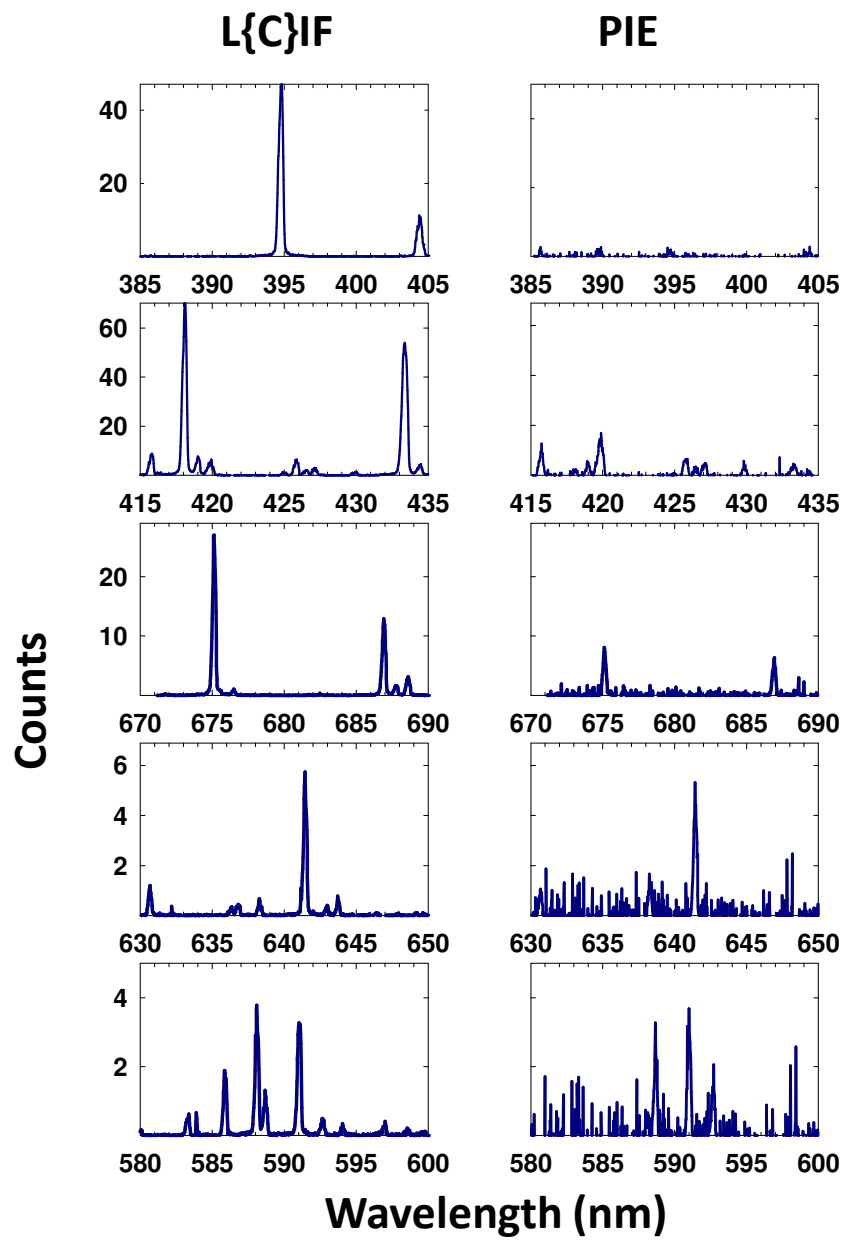


Figure 8

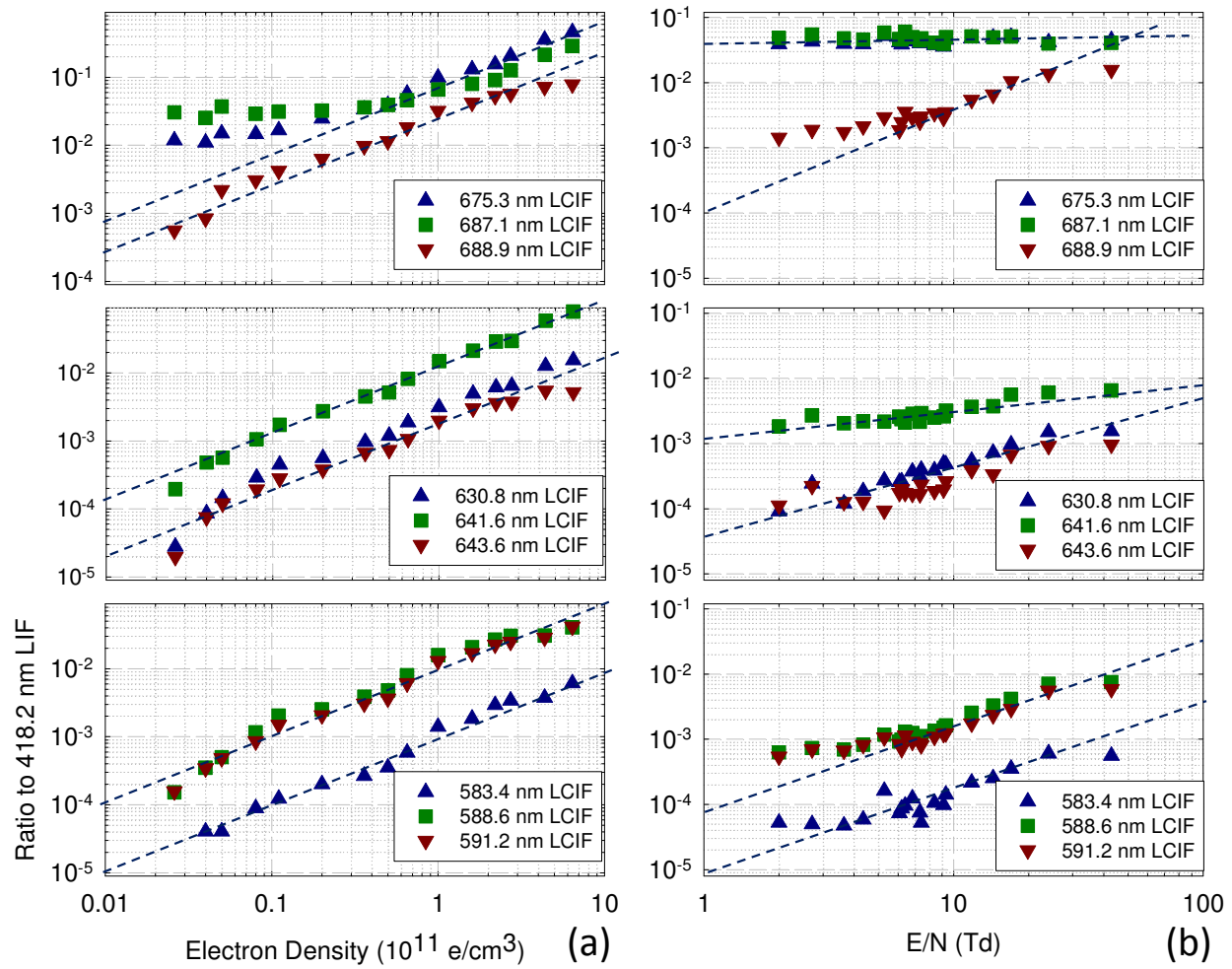


Figure 9



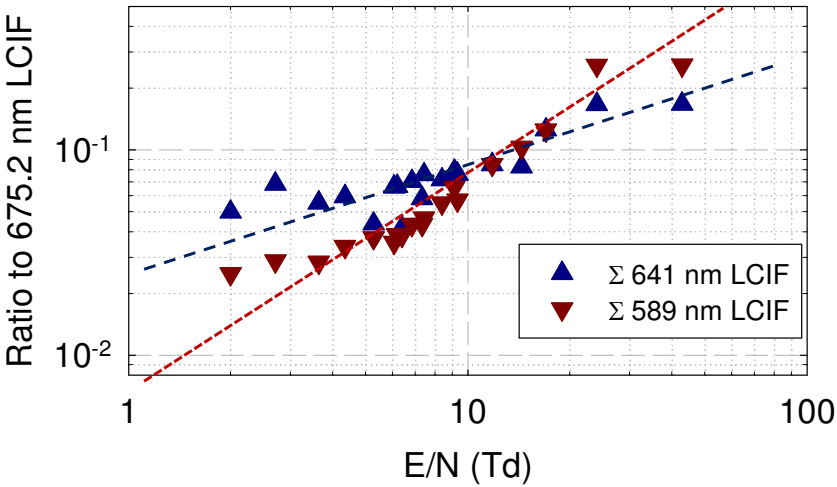


Figure 10

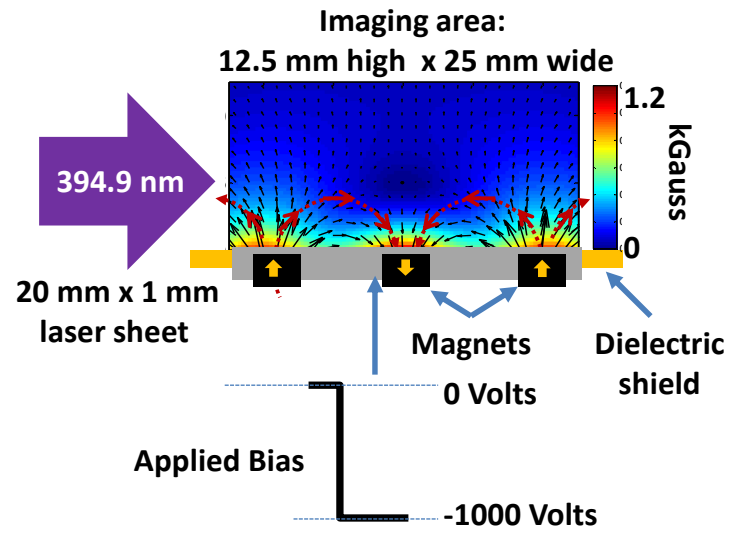
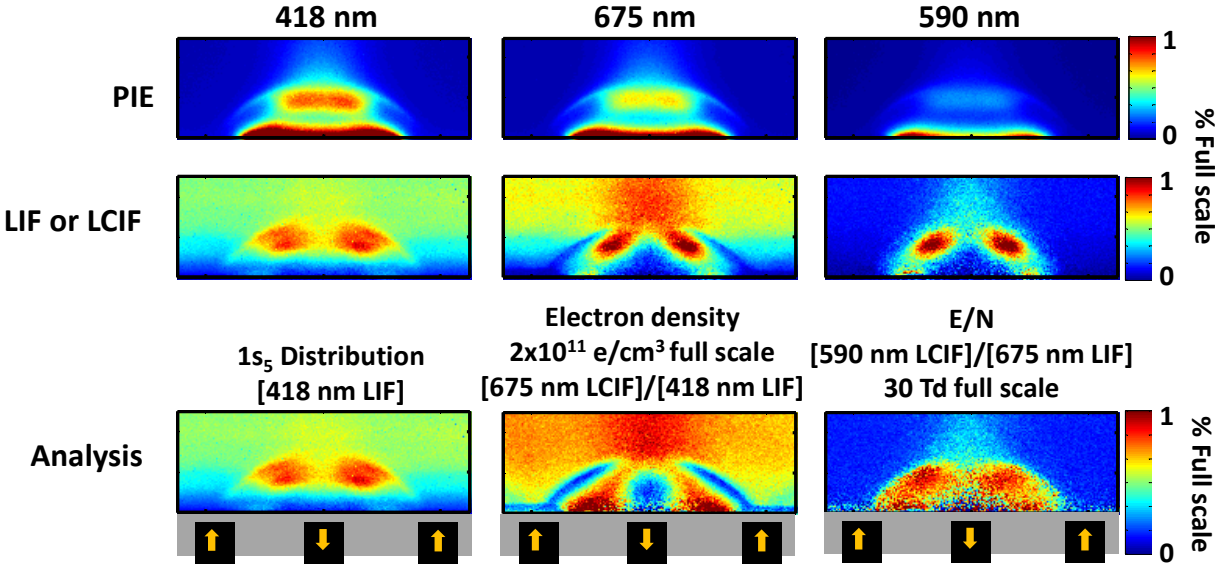


Figure 11



Imaging area: 12.5 mm high x 25 mm wide

Figure 12